# Spin-degenerate regimes for single quantum dots in transition metal dichalcogenide monolayers

Matthew Brooks* and Guido Burkard
*Department of Physics, University of Konstanz, D-78464 Konstanz, Germany*
(Received 17 March 2017; published 12 June 2017)

Strong spin-orbit coupling in transition metal dichalcogenide (TMDC) monolayers results in spin-resolvable band structures about the $K$ and $K'$ valleys such that the eigenbasis of a two-dimensional quantum dot (QD) in a TMDC monolayer in zero field is described by the Kramers pairs $|0\rangle_- = |K'\uparrow\rangle$, $|1\rangle_- = |K\downarrow\rangle$ and $|0\rangle_+ = |K\uparrow\rangle$, $|1\rangle_+ = |K'\downarrow\rangle$. The strong spin-orbit coupling limits the usefulness of single TMDC QDs as spin qubits. Possible regimes of spin-degenerate states, overcoming the spin-orbit coupling in monolayer TMDC QDs, are investigated in both zero field, where the spin and valley degrees of freedom become fourfold degenerate, and twofold degeneracy in some magnetic field, localized to a given valley. Such regimes are shown to be achievable in $MoS_2$, where the spin-orbit coupling is sufficiently low and of the right sign such that the spin-resolved conduction bands intersect at points about the $K$ and $K'$ valleys and as such may be exploited by selecting suitable critical dot radii.

DOI: 10.1103/PhysRevB.95.245411

## I. INTRODUCTION

Transition metal dichalcogenide (TMDC) monolayers are atomically thin crystal layers exfoliated down from bulk weakly cohesive stacks. Similar to graphene, a hexagonal lattice of alternating lattice sites results in two inequivalent, time-reversal-symmetric valleys [$K$ and $K'$; see Fig. 1(b)] [1–4]. Unlike graphene, the monolayer crystals possess broken inversion symmetry [see Fig. 1(a)], inducing direct band gaps in the visible range about the two valleys [5–7]. Furthermore, strong spin-orbit coupling from the transition metal atoms introduces a strong coupling between the spin and valley degrees of freedom [see Fig. 1(a)] [8–10]. TMDCs are characterized by the chemical composition $MX_2$, where $M$ denotes the transition metal (Mo or W) and $X$ denotes the chalcogenide (S or Se). The presence of a direct band gap and spin-valley coupling in a two-dimensional material allows for a number of interesting electronic, spintronic, and valleytronic applications, including room-temperature quantum spin Hall insulators, optically pumped valley polarization, long-lived exciton spin polarization, and two-dimensional (2D) quantum dots (QDs) [11–16].

While the strong spin-valley coupling of TMDC monolayers offers numerous interesting physical phenomena, it presents a difficulty for qubit implementation in gated QDs. Kramers pairs of the spin and valley degrees of freedom result from this coupling [13,14,17]. At low energy the $|0\rangle_- = |K'\uparrow\rangle$ and $|1\rangle_- = |K\downarrow\rangle$ states are degenerate in zero field and are energetically separate from the $|0\rangle_+ = |K\uparrow\rangle$ and $|1\rangle_+ = |K'\downarrow\rangle$ states [14,18,19]. This effect can be observed in the spin-resolvable structure of the conduction band (CB) about the $K$ and $K'$ points [20,21], as shown in Fig. 1(c). The obvious choice for the computational basis of a qubit is therefore a spin-valley qubit consisting of the two states of the lowest-lying Kramers pair, $|0\rangle_-$ ($|1\rangle_-$) in $MoX_2$ and $|0\rangle_+$ ($|1\rangle_+$) in $WX_2$, where the required energy difference may be achieved by spin-valley Zeeman splitting induced by a perpendicular magnetic field [22–25]. However, such qubits are inherently limited by a necessity for coupling of the valley states. Methods of doing so have been proposed in carbon nanotubes by means of short-range disorder in the dots [22,26], requiring atomic-level engineering, or by optical manipulation [27]. Additionally, the valley coherence of $WSe_2$ excitons has been measured [28], demonstrating an order of magnitude lower coherence times than spin in other TMDC monolayer crystals [11]. If qubits in TMDC monolayers could operate similarly to semiconductor spin qubits, then the broad theoretical and experimental findings of the field [29–31] could be directly utilized. In so doing, a novel breed of 2D, optically active, direct band gap, and relatively nuclear spin free [15] semiconductor spin qubits would be gained without the need for an artificially induced band gap, as is needed in graphene [32]. This requires a method of manipulating the dots such that the spin-orbit coupling may be suppressed and regimes of pure spin qubits may be accessed.

There is a noticeable and useful difference between the low-energy band structures of Mo-based and W-based monolayers, as demonstrated in Fig. 1(c): the band crossings observed in the spin-resolved CB structures in Mo monolayers are absent in W monolayers, which suggests that it is possible to achieve spin degeneracy localized within a given valley. Such spin-degenerate regimes offer the possibility of implementing the desired pure spin qubits in TMDCs. Additionally, by placing a TMDC material in a perpendicular magnetic field, breaking time-reversal symmetry, valley Zeeman splitting may be introduced to the system. Previous work [14] has suggested that it may be possible to access regimes of spin degeneracy within the same valley by introducing a large magnetic field. In this work, we build upon previous analyses of TMDC QDs in an effective low-energy regime by solving for various conditions in which a spin qubit may be viable, demonstrating a dot-size-tunable spin-orbit splitting and investigating the effects of a finite-potential well model as opposed to previous assumptions of an infinite potential.

Here, we present methods of achieving spin degeneracy within a given valley of a QD in a TMDC monolayer at zero or moderate fields. First, in Sec. II a zero-external-field model is discussed, demonstrating the Kramers pairing of states to derive an expression for a critical radius at which fourfold

*matthew.brooks@uni-konstanz.de

 

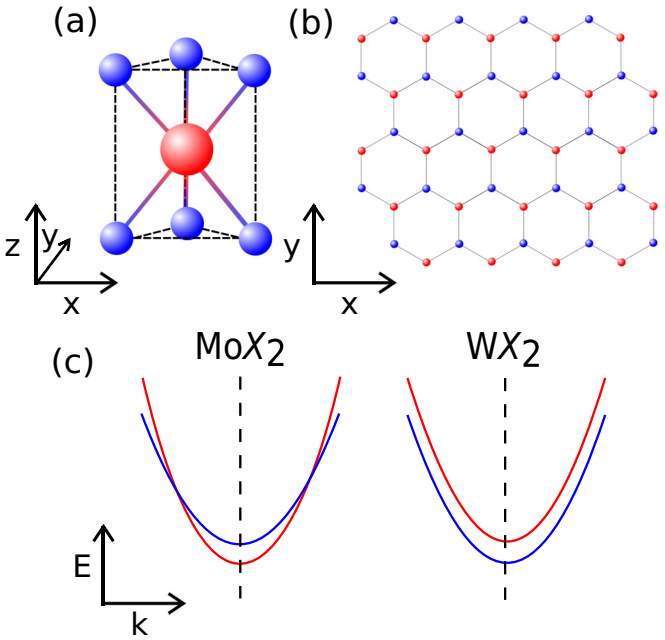


FIG. 1. (a) Three-dimensional view of a TMDC unit cell (red denoting $M$ atoms, blue denoting $X$ atoms) showing the three sublayers of a TMDC monolayer and the broken inversion of the crystal lattice. (b) Planar ($X$-$Y$) view of a TMDC lattice. (c) Spin-resolved conduction band (red: $|0\rangle_- = |K'\uparrow\rangle$ and $|1\rangle_- = |K\downarrow\rangle$, blue: $|0\rangle_+ = |K\uparrow\rangle$ and $|1\rangle_+ = |K'\downarrow\rangle$) around the $K$ valley in the BZ of Mo- and W-based TMDC monolayers demonstrating the spin crossings present in Mo TMDCs and not in W; the $K'$ valley may be visualized simply by the time reversal of the given band structure.

spin-valley degeneracy may be expected. Also we discuss the best candidate monolayer for a pure spin qubit. Then in Sec. III an external magnetic field perpendicular to the dot is considered, and numerical solutions to the necessary external field strengths at a given dot radius are shown at which a spin-degenerate state within a given valley is expected. Next, the effects of the finite confinement potential on the two previously discussed regimes are given in Sec. IV. Finally, an effective implementation regime for the various methods of achieving valley-independent spin degeneracy is discussed in Sec. V before a summary is given in Sec. VI.

## II. ZERO FIELD

To describe a QD in monolayer TMDC the following effective low-energy Hamiltonian about the $K$ and $K'$ points in the CB is employed [14]:

$$H_{\rm dot} = H_{\rm el}^{\tau,s} + H_{\rm so}^{\rm intr} + V = \frac{\hbar^2 q_+ q_-}{2m_{\rm eff}^{\tau,s}} + \tau\Delta_{\rm cb}s_z + V. \quad (1)$$

Here, $\tau = 1\,(-1)$ refers to the $K$ ($K'$) valley, $s_z$ gives the spin Pauli $z$ matrix with eigenvalues $s = 1\ (-1)$ for spin $\uparrow$ ($\downarrow$), wave number operators $q_\pm = q_x \pm iq_y$, where $q_k = -i\partial_k$, $\Delta_{cb}$ is the energy splitting in the CB due to the strong intrinsic spin-orbit coupling of the TMDC monolayer, and the spin-valley-dependent effective electron mass is defined as $1/m_{\rm eff}^{\tau,s} = 1/m_{el}^0 - \tau s/\delta m_{\rm eff}$, where $\delta m_{\rm eff}$ is material dependent. Initially, it is assumed that the QD potential $V$ is sufficiently deep that it may be described by an infinite hard-walled potential,

$$V = \begin{cases} 0 & r \leqslant R_D, \\ \infty & r > R_D, \end{cases} \quad (2)$$

where $r$ is the radial coordinate and $R_D$ is the radius of the dot. This may be assumed in lieu of a harmonic potential, as is often used in bulk semiconductor QD models since the 2D nature of a TMDC allows for a more direct interface between the gates and the plane in which an electron will be confined. Additionally, such an assumption allows for edge effects at the boundary of the dot to be neglected. In 2D polar coordinates, the wave-number operators may be defined as

$$q_\pm = \pm ie^{\pm i\phi}\left(\mp\partial_r - \frac{i}{r}\partial_\phi\right), \quad (3)$$

where $\phi$ is the angular coordinate. Assuming the dot is circular, rotational symmetry about the $z$ axis dictates that the dot's Hamiltonian will commute and share eigenstates with the $z$ component of the angular momentum operator $l_z$. This allows for the normalized solution of the angular component of the wave function $\Psi(r,\phi) = R(r)\Phi(\phi)$ to be given as

$$\Phi(\phi) = \frac{e^{il\phi}}{\sqrt{2\pi}}. \quad (4)$$

Since the radial component of the wave function observes the boundary condition $R(R_D) = 0$, the following expression is derived, where $j_{n,l}$ is the $n$th zero ($n = 1,2,3,\dots$) of the $l$th Bessel function of the first kind $J_l$ ($l = 0,\pm1,\pm2,\dots$):

$$R_{n,l}(r) = \frac{(-1)^{\frac{|l|-l}{2}}\sqrt{2}J_{|l|}\left(\frac{j_{n,|l|}}{R_D}r\right)}{R_D j_{n,|l|+1}}. \quad (5)$$

As such, the full normalized solutions of a hard-wall TMDC quantum dot in zero external field are given in the spinor form as

$$\Psi_{n,l}^{\uparrow}(r,\phi) = \frac{e^{il\phi}}{\sqrt{2\pi}}\begin{pmatrix}1\\0\end{pmatrix}R_{n,l}(r), \quad (6a)$$

$$\Psi_{n,l}^{\downarrow}(r,\phi) = \frac{e^{il\phi}}{\sqrt{2\pi}}\begin{pmatrix}0\\1\end{pmatrix}R_{n,l}(r), \quad (6b)$$

and the spin, valley, and dot-radius-dependent energy eigenvalues are given as

$$E_{\tau,s}^{n,l}(R_D) = \frac{\hbar^2 j_{n,|l|}^2}{2m_{\rm eff}^{\tau,s}R_D^2} + \tau s\Delta_{\rm cb}. \quad (7)$$

From the four realizations of spin and valley, only two separate energy solutions in zero field emerge, i.e., $E_{K,\uparrow}^{n,l} = E_{K',\downarrow}^{n,l} = E_+^{n,l}$ and $E_{K',\uparrow}^{n,l} = E_{K,\downarrow}^{n,l} = E_-^{n,l}$. These two possible solutions describe the $|0\rangle_+$ ($|1\rangle_+$) and $|0\rangle_-$ ($|1\rangle_-$) Kramers pairs, respectively. If the two solutions are assumed to be equivalent, then Eq. (7) may be used to describe the radius at which fourfold degeneracy in the valley-spin Hilbert space is achieved. As such, a critical radius $R_c^{n,l}$ at which $E_+^{n,l} = E_-^{n,l}$ is given by

$$R_{\rm c}^{n,l} = \frac{\hbar j_{n,|l|}}{2\sqrt{\Delta_{\rm cb}}}\sqrt{\frac{1}{m_{\rm eff}^-} - \frac{1}{m_{\rm eff}^+}}, \quad (8)$$

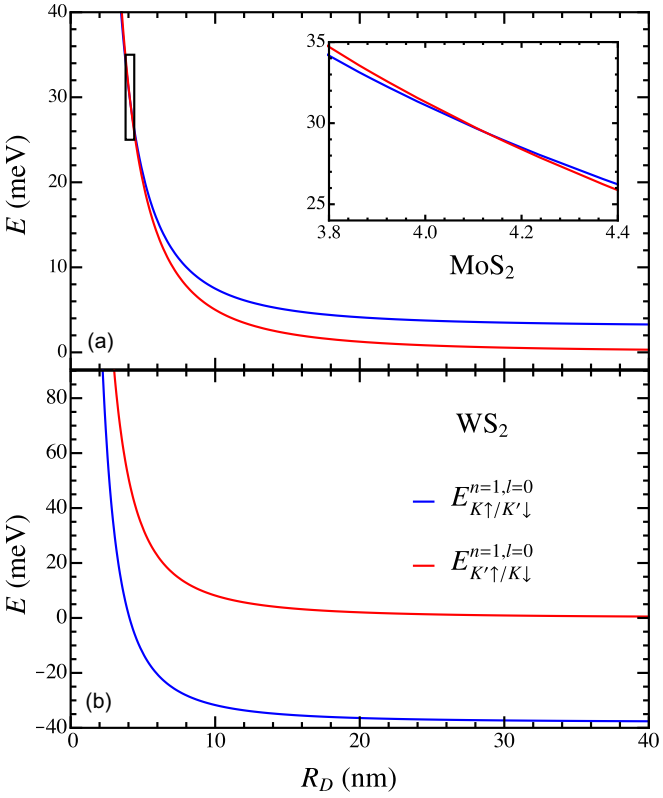


FIG. 2. (a) Zero-field energy spectrum of the $n = 1, l = 0$ eigenstates [blue: $|0\rangle_+$ ($|1\rangle_+$) and red: $|0\rangle_-$ ($|1\rangle_-$)] of a $MoS_2$ hard-wall QD of a given dot radius $R_D$; here, a point of fourfold degeneracy of the valley-spin eigenstates is observed at a particular radius. Inset: region about which the fourfold degeneracy is observed in the spectrum. (b) Zero-field energy spectrum of the $n = 1, l = 0$ eigenstates of a $WS_2$ hard-wall QD of a given dot radius; here, no point of fourfold degeneracy of the valley-spin eigenstates is observable due to the $\Delta_{cb} > 0$ not being satisfied by W-based TMDCs.

where $m^-_{\rm eff} = m^{K\downarrow/K'\uparrow}_{\rm eff}$ and $m^+_{\rm eff} = m^{K\uparrow/K'\downarrow}_{\rm eff}$. Therefore, there are real solutions to the critical radius at which fourfold valley-spin degeneracy may exist for dots with intrinsic spin-orbit coupling such that $\Delta_{cb} > 0$ and $m^+_{\rm eff} > m^-_{\rm eff}$. The latter condition is given for all possible TMDC monolayers, while the former is only satisfied by Mo-based TMDCs ($\Delta_{cb} =$ 1.5 meV for $MoS_2$ and $\Delta_{cb} = 11.5$ meV for $MoSe_2$; see Fig. 2) [4,14]. Alternatively, real solutions of $R_c$ may be found in materials where both $\Delta_{cb} < 0$ and $m^+_{\rm eff} < m^-_{\rm eff}$; however, there is no known TMDC that satisfies the latter condition.

In the ground state ($n = 1, l = 0$) the critical radius at which fourfold degeneracy may be expected is 4.13 nm for $MoS_2$ and 1.46 nm for $MoSe_2$ QDs. While both radii are difficult to achieve by electrostatic gating, $MoS_2$ monolayers offer plausibly achievable fourfold degeneracy through some critical radii and, consequently, prove themselves to be the most viable candidate for 2D single-QD pure spin qubits. For the remainder of the present work we will focus solely on $MoS_2$ monolayers.

## III. PERPENDICULAR MAGNETIC FIELD

Following the previous methods [14], the spin-valley eigenenergies of a TMDC monolayer QD in a constant perpendicular magnetic field $B_z$ may be derived from the following Hamiltonian:

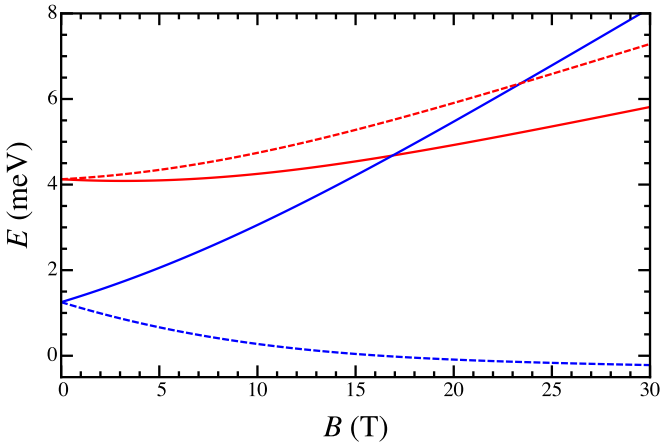


FIG. 3. Energy spectra of the $n = 1, l = 0$ state in a QD of 20 nm radius on a $MoS_2$ monolayer under a perpendicular magnetic field. Here, the critical field strength at which $E^{n=1,l=0}_{K',\downarrow} = E^{n=1,l=0}_{K',\uparrow}$ is observed at the high magnetic field strength of ~23 T. The blue solid (dashed) line shows $|K'\uparrow\rangle$ ($|K\downarrow\rangle$), and the red solid (dashed) line shows $|K\uparrow\rangle$ ($|K'\downarrow\rangle$).

$$H^{\tau,s}_{B_\perp} = \hbar\omega^{\tau,s}_c\alpha_+\alpha_- + \tau\Delta_{\rm cb}s_z + \frac{1+\tau}{2}\frac{B_z}{|B_z|}\hbar\omega^{\tau,s}_c + \frac{1}{2}(\tau g_{\rm vl} + g_{\rm sp}s_z)\mu_B B_z, \quad (9)$$

where the cyclotron frequency is defined as $\omega^{\tau,s}_c = e|B_z|/m^{\tau,s}_{\rm eff}$, $\mu_B$ is the Bohr magneton, $g_{sp}$ is the spin $g$ factor, $g_{vl}$ is the valley $g$ factor, and $\alpha_\pm$ denote the modified wave-number operators $\alpha_\pm = \mp il_B q_\pm/\sqrt{2}$, where $l_B = \sqrt{\hbar/eB_z}$ is the magnetic length. After appropriate gauge selection wave functions in terms of the dimensionless length parameter $\rho = r^2/2l_B^2$ are given as $P_{n,l}(\rho) = \rho^{|l|/2}e^{-\rho/2}M(a_{n,l},|l|+1,\rho)$, where $a_{n,l}$ describes the $n$th solution of the bound-state identity $M(a_{n,l},|l|+1,\rho_D) = 0$, where $\rho_D = \rho[r = R_D]$ and $M(a,b,c)$ is the confluent hypergeometric function of the first kind. The addition of an out-of-plane magnetic field does not break the rotational symmetry of the dot; hence, the angular component of the wave function is not affected by this change. The eigenenergies are therefore given as

$$E^{\tau,s}_{n,l} = \hbar\omega^{\tau,s}_c\left(\frac{1+\tau}{2}\frac{B_z}{|B_z|} + \frac{|l|+l}{2} - a_{n,l}\right) + \tau\Delta_{\rm cb}s_z + \frac{1}{2}(\tau g_{\rm vl} + sg_{\rm sp})\mu_B B_z. \quad (10)$$

From Eq. (10), spectra demonstrating the effect of an out-of-plane magnetic field for QDs in $MoS_2$ monolayers may be calculated numerically. The splitting of the spin and valley states due to the external magnetic field allows for spin-degenerate crossings for a given radius within the $K'$ valley, i.e., at some external magnetic field strength $E^{n,l}_{K',\uparrow} = E^{n,l}_{K',\downarrow}$ (see Fig. 3). These critical magnetic field strengths $B_c$ for given dot radii may be determined for a range of radii to give the spin-degenerate regime spectra shown in Fig. 4.

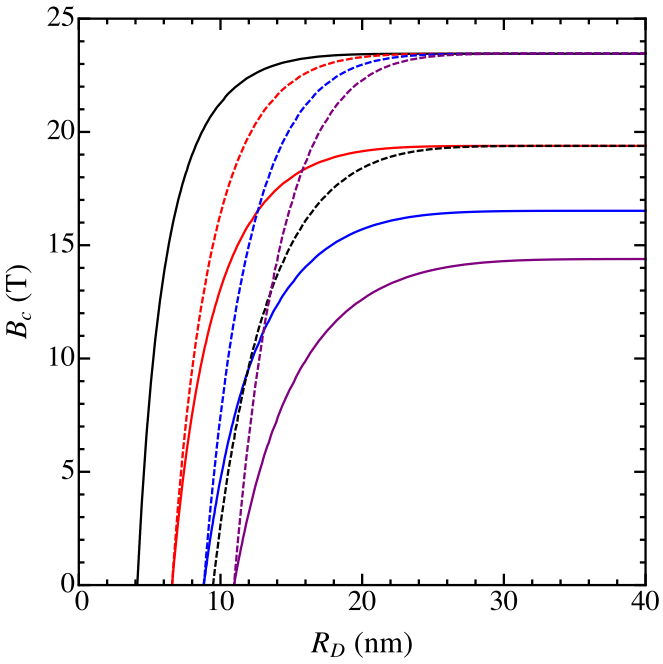


FIG. 4. Spin-degeneracy curves of critical out-of-plane magnetic field strength $B_c$ with the radius of a QD on a $MoS_2$ monolayer for the first few states; the black solid (dashed) line shows $n = 1$ (2), $l = 0$, the red solid (dashed) line shows $n = 1, l = 1$ $(-1)$, the blue solid (dashed) line shows $n = 1, l = 2$ $(-2)$, and the purple solid (dashed) line shows $n = 1, l = 2$ $(-2)$.

These spectra show separate plateaus in the critical field strength at relatively high dot radii ($R > 20$ nm) for the $l \geqslant 0$ and $l < 0$ angular states, differing by up to $\sim$5 T, but with both still at high field strengths. This is the limit at which the maximum Kramers pair energy difference at zero field is observed and valley Zeeman splitting alone is used to achieve spin degeneracy. On the other end of the spectra, at low external field strengths the gradient of the regime curves increases, compromising the fabrication error robustness of single-dot spin qubits; that is, small errors ($\sim$1 nm) in QD radii would make the difference between operating the qubit at 1- and 6-T external field. Thus, operating a spin qubit with a single-electron regime in the ground state is not easily implemented. The possibility of operation at excited states and alternative enhancement methods are considered and discussed in Sec. V.

## IV. FINITE WELL

Up to this point, all models used assume QDs with an infinite hard-wall potential. Here, the effects of transitioning to a finite hard-wall potential

$$V = \begin{cases} 0 & r \leqslant R_D, \\ V_0 & r \geqslant R_D, \end{cases} \tag{11}$$

on the spin-degenerate regimes discussed are shown. Thus, for both the zero-field and perpendicular-magnetic-field regimes, the $\Psi(r = R_D, \phi) = 0$ boundary condition is replaced by the continuity condition at the potential interface $\partial_r \ln[\Psi_{n,l}^{r \geqslant R_D}(r = R_D, \phi)] = \partial_r \ln[\Psi_{n,l}^{r \leqslant R_D}(r = R_D, \phi)]$ [33].

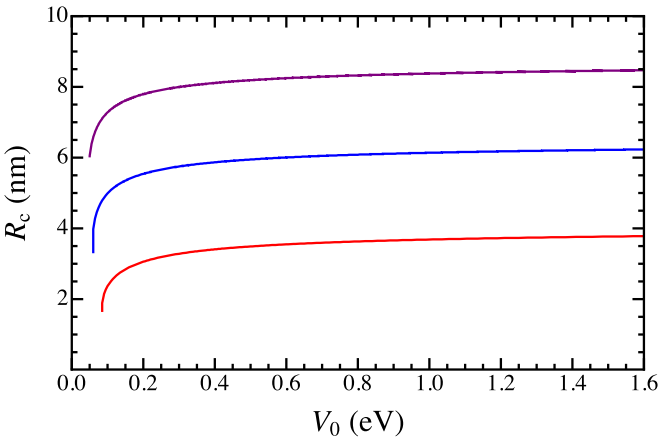


FIG. 5. Spin-degenerate critical radii $R_c$ of QD of finite potential height in $MoS_2$ monolayers at the ground and first few excited states, red: $n = 1, l = 0$, blue: $n = 1, |l| = 1$, purple: $n = 1, |l| = 2$.

In zero field the unnormalized radial portions of the wave function within and outside of the potential barrier are described as follows:

$$R_{n,l}(r) = \begin{cases} J_{|l|}(\epsilon_{n,l}^{\text{in}} r) & r \leqslant R_D, \\ e^{\frac{il\pi}{2}} K_{|l|}(\epsilon_{n,l}^{\text{out}} r) & r \geqslant R_D. \end{cases} \tag{12}$$

Here, $K_l$ is the $l$th modified Bessel function of the second kind, $\epsilon_{n,l}^{\text{in}} = \sqrt{2m_{\text{eff}}^{\tau,s}[E_{n,l} - \tau\Delta_{\text{cb}} s_z]}/\hbar$, and $\epsilon_{n,l}^{\text{out}} = \sqrt{2m_{\text{eff}}^{\tau,s}[V_0 - E_{n,l} + \tau\Delta_{\text{cb}} s_z]}/\hbar$. Eigenenergies as a function of potential height may then be numerically calculated by applying the continuity condition to Eq. (12),

$$\frac{\epsilon_{n,l}^{\text{in}} J_{|l|+1}(\epsilon_{n,l}^{\text{in}} R_D)}{J_{|l|}(\epsilon_{n,l}^{\text{in}} R_D)} = \frac{\epsilon_{n,l}^{\text{out}} K_{|l|+1}(\epsilon_{n,l}^{\text{out}} R_D)}{K_{|l|}(\epsilon_{n,l}^{\text{out}} R_D)}. \tag{13}$$

From this, the fourfold-degenerate critical radii as a function of potential height may be calculated, leading to the result shown in Fig. 5. The effect of a finite potential is noticeable only at low potential heights, $<$100 meV, whereafter a sharp drop in the critical radii is observed.

Similarly, when a finite potential is considered with an external magnetic field over the QD, the unnormalized radial component of the wave function is described as

$$P_{n,l}(\rho) = \rho^{|l|/2} e^{-\rho/2} \begin{cases} M(\tilde{a}_{n,l}^{\text{in}}, |l| + 1, \rho) & r \leqslant R_D, \\ U(\tilde{a}_{n,l}^{\text{out}}, |l| + 1, \rho) & r \geqslant R_D, \end{cases} \tag{14}$$

where $U(\tilde{a}_{n,l}^{\text{out}}, |l| + 1, \rho)$ is Tricomi's hypergeometric function, $\tilde{a}_{n,l}^{\text{in}}$ is the $n$th numerical solution to the continuity equation at the potential barrier, and $\tilde{a}_{n,l}^{\text{out}} = \tilde{a}_{n,l}^{\text{in}} + V_0/\hbar\omega_c^{\tau,s}$. The continuity condition may then be applied to achieve the following characteristic equation:

$$\begin{aligned}(1 + |l|)\tilde{a}_{n,l}^{\text{out}} M(\tilde{a}_{n,l}^{\text{in}}, |l| + 1, \rho_D) U(1 + \tilde{a}_{n,l}^{\text{out}}, |l| + 2, \rho_D) \\ + \tilde{a}_{n,l}^{\text{in}} M(1 + \tilde{a}_{n,l}^{\text{in}}, |l| + 2, \rho_D) U(\tilde{a}_{n,l}^{\text{out}}, |l| + 1, \rho_D) = 0,\end{aligned} \tag{15}$$

from which $\tilde{a}_{n,l}^{in}$ may be numerically extracted and applied to Eq. (10) in lieu of $a_{n,l}$. The effect of a finite-potential-height model on the spin-degenerate regimes of $MoS_2$ is shown in Fig. 6.

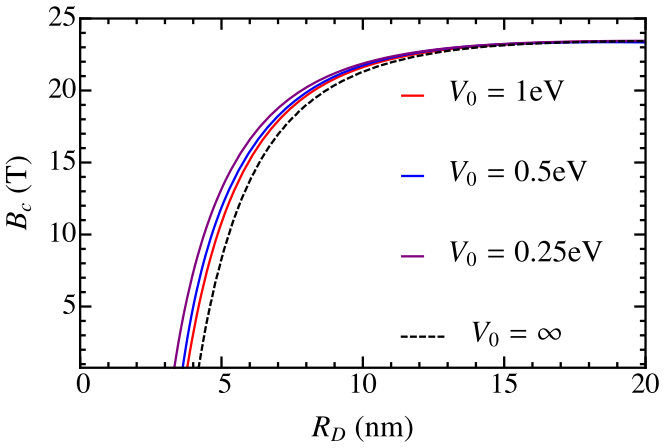


FIG. 6. Spin-degenerate critical magnetic field $B_c$ of QDs of finite potential heights in $MoS_2$ monolayers at the ground of heights 1 eV (red line), 0.5 eV (blue line), and 0.25 eV (purple line) and infinite potential (black dashed line) for reference.

A similar effect on the spin-degeneracy regimes is shown in both Figs. 5 and 6. At shallow potential heights the required critical radius of the dot decreases by ∼1–2 nm. However, at high magnetic field, there is no discernible difference between the finite- and infinite-potential solutions. This result poses little threat to the operation of dots with a single electron charged into the ground state as the potential height may be selected to be sufficiently high such that little to no difference in the critical radii will be observed. However, as discussed in Sec. V, this effect must be considered when switching to an excited operational electron state by charging.

## V. SINGLE QUANTUM DOTS AS QUBITS

To achieve a pure spin qubit in a single $MoS_2$ QD, some considered parameter selection is required to gain a certain robustness of the operational regime. As previously stated in Sec. III, a regime with a single electron in the lowest spin-degenerate state requires either a very large external field ($> 20$ T) or extreme precision in the QD's radius. This is not ideal; however, these problems may be mitigated by charging the dot to operate at higher degenerate states. As can be seen in Fig. 4, at reasonable external fields ($\leqslant 10$ T), for each increasing excited state the necessary QD radius increases in accordance with Eq. (8). These regimes allowing for larger dot radii are more reliably achieved by gated monolayer QD fabrication methods. Moreover, the $(|l| + l)/2$ term of Eq. (10) splits the plateaus of the regime curves shown in Fig. 4 into the higher plateaus of the $l \leqslant 0$ and lower $l = 1,2,\ldots$ plateaus. Therefore, if a charged excited state is chosen as the operational state, the ideal choice would be an $l > 0$ angular state.

Even in the lowest spin-degenerate state, some charging may be required. The operational electron confined to the $K'$ valley is at a higher energy than the two other possible states in the $K$ valley (see Fig. 3). Although valley lifetime is expectedly long [11,34], eventually, the electron will decay out of the higher operational state to these empty states. Also, since each excitation state may be split into four different configurations of spin and valley, the total number of electrons needed to charge the dot up to the desired operational regime is $3 + 4N$, where $N$ is an integer describing the excitation level of the operational state; that is, $N = 0$ corresponds to the ground state $n = 1, l = 0$, $N = 1$ corresponds to the first excited state $n = 1, l = -1$, etc. The direct band gap of monolayer $MoS_2$ is ∼1.8 eV [6], and current advances in gated QD nanostructures in $MoS_2$ give a charging energy of 2 meV at a dot radius of 70 nm [35]. This result has been said to align well with the self-capacitance model [29,35,36]; therefore, using said model, the charging energy at desired radii for spin-degenerate regimes (∼10 nm) may be approximately shown to increase to ∼14 meV. This is, however, a broad approximation; therefore, further study of the perturbation of the energy levels due to Coulomb interaction mediated by the Keldysh potential [37] is warranted. However, such effects are spin and valley independent and should serve only as a renormalization of the effects studied here. These considerations do, however, limit the choice of excited operational states; as is evident in Fig. 5, at highly charged states relative to the potential height and band gap, the critical radii will be compromised.

Additionally, ferromagnetic substrates may be employed to enhance the valley splitting due to an external magnetic field. Recent experiments have demonstrated an effective ∼2 T addition to the magnetic field inducing valley Zeeman splitting in $WSe_2$ monolayers on a EuS ferromagnetic substrate [38]. Such techniques may be employed to reduce the necessary external field strength to reasonable quantities.

An alternative quantum confinement method with TMDC monolayers has been proposed by way of heterostructures consisting of islands of one form of Mo-based TMDC within a sea of the corresponding W-based monolayer [15,39] or by sufficiently small free-standing flakes [40]. While such methods offer quantum confinement on the desired scale, high-intervalley-coupling terms are introduced at small dot radii due to edge effects, offering a decoherence channel to the system. Additionally, such structures offer scalability challenges such as the lack of a method to adjust the exchange coupling if the proposed model is extended to a double-QD system. However, such studies of quantum confinement in TMDCs pay close attention to the effect of dot shape, a consideration that was omitted here for simple symmetry considerations but could yet warrant consideration in further research.

With a suitable operational regime selected, operation of the spin qubit is relatively straightforward. The energy gap between the up- and down-spin computational bases is tunable by the external magnetic field, while Bychkov-Rashba spin-orbit coupling induced by an external electric field perpendicular to the device may be used to provide off-diagonal spin-coupling terms in the spin Hilbert space [14].

## VI. SUMMARY

Overall, given selection of a proper operational regime and reasonable accuracy in QD fabrication at low radii, $MoS_2$ monolayer QDs do offer novel pure spin qubits in 2D semiconductors. Overcoming the Kramers pairs of gated QDs on TMDC monolayers was explored to achieve operational regimes of pure spin qubits, thus avoiding the problem of achieving valley state mixing and low valley coherence times.

Zero-field fourfold spin-valley degeneracy was demonstrated to be achievable in Mo-based TMDC monolayers, unlike their W-based counterparts, at low QD radii, while spin degeneracy solely within a given valley was shown to be achieved by application of a sufficiently high external magnetic field perpendicular to the dot. Regime restrictions for spin-degenerate $MoS_2$ QDs have been shown, demonstrating radially sensitive low-external-field regimes which may be made to be more robust when charged into higher operational states and enhanced valley-Zeeman-splitting substrates. Switching from an infinite- to a finite-potential barrier model did demonstrate a drop in the expected values of spin-degenerate critical radii but only at particularly low barrier heights. In addition to the moderate expected charging energy this somewhat limits the usefulness of highly charged operational states but will not substantially affect operation at the first few excited states. To conclude, a theoretical demonstration of QD-radius-dependent spin-orbit effects in TMDC monolayers was given along with descriptions of possible methods to implement novel pure spin qubits on two-dimensional semiconductor crystals.

## ACKNOWLEDGMENTS

We acknowledge helpful discussions with A. Kormányos, A. Pearce, M. Rančić, and M. Russ and funding from both the European Union by way of the Marie Curie ITN Spin-Nano and the DFG through SFB 767.

[1] Q. H. Wang, K. Kalantar-Zadeh, A. Kis, J. N. Coleman, and M. S. Strano, Nat. Nanotechnol. **7**, 699 (2012).
[2] R. Suzuki, M. Sakano, Y. Zhang, R. Akashi, D. Morikawa, A. Harasawa, K. Yaji, K. Kuroda, K. Miyamoto, T. Okuda *et al.*, Nat. Nanotechnol. **9**, 611 (2014).
[3] T. Cao, G. Wang, W. Han, H. Ye, C. Zhu, J. Shi, Q. Niu, P. Tan, E. Wang, B. Liu, and J. Feng, Nat. Commun. **3**, 887 (2012).
[4] A. Kormányos, G. Burkard, M. Gmitra, J. Fabian, V. Zólyomi, N. D. Drummond, and V. Fal'ko, 2D Mater. **2**, 022001 (2015).
[5] A. Splendiani, L. Sun, Y. Zhang, T. Li, J. Kim, C.-Y. Chim, G. Galli, and F. Wang, Nano Lett. **10**, 1271 (2010).
[6] K. F. Mak, C. Lee, J. Hone, J. Shan, and T. F. Heinz, Phys. Rev. Lett. **105**, 136805 (2010).
[7] H.-Z. Lu, W. Yao, D. Xiao, and S.-Q. Shen, Phys. Rev. Lett. **110**, 016806 (2013).
[8] D. Xiao, G.-B. Liu, W. Feng, X. Xu, and W. Yao, Phys. Rev. Lett. **108**, 196802 (2012).
[9] W.-Y. Shan, H.-Z. Lu, and D. Xiao, Phys. Rev. B **88**, 125301 (2013).
[10] X. Xu, W. Yao, D. Xiao, and T. F. Heinz, Nat. Phys. **10**, 343 (2014).
[11] L. Yang, N. A. Sinitsyn, W. Chen, J. Yuan, J. Zhang, J. Lou, and S. A. Crooker, Nat. Phys. **11**, 830 (2015).
[12] Y. Ma, L. Kou, X. Li, Y. Dai, and T. Heine, Phys. Rev. B **93**, 035442 (2016).
[13] M. Cazalilla, H. Ochoa, and F. Guinea, Phys. Rev. Lett. **113**, 077201 (2014).
[14] A. Kormányos, V. Zólyomi, N. D. Drummond, and G. Burkard, Phys. Rev. X **4**, 011034 (2014).
[15] Y. Wu, Q. Tong, G.-B. Liu, H. Yu, and W. Yao, Phys. Rev. B **93**, 045313 (2016).
[16] H. Zeng, J. Dai, W. Yao, D. Xiao, and X. Cui, Nat. Nanotechnol. **7**, 490 (2012).
[17] J. Klinovaja and D. Loss, Phys. Rev. B **88**, 075404 (2013).
[18] Y. Song and H. Dery, Phys. Rev. Lett. **111**, 026601 (2013).
[19] A. Kormányos, V. Zólyomi, N. D. Drummond, P. Rakyta, G. Burkard, and V. I. Fal'ko, Phys. Rev. B **88**, 045416 (2013).
[20] K. Kośmider, J. W. González, and J. Fernández-Rossier, Phys. Rev. B **88**, 245436 (2013).
[21] Z. Zhu, Y. Cheng, and U. Schwingenschlögl, Phys. Rev. B **84**, 153402 (2011).
[22] K. Flensberg and C. M. Marcus, Phys. Rev. B **81**, 195418 (2010).
[23] G. Aivazian, Z. Gong, A. M. Jones, R.-L. Chu, J. Yan, D. G. Mandrus, C. Zhang, D. Cobden, W. Yao, and X. Xu, Nat. Phys. **11**, 148 (2015).
[24] A. Srivastava, M. Sidler, A. V. Allain, D. S. Lembke, A. Kis, and A. Imamoğlu, Nat. Phys. **11**, 141 (2015).
[25] H. Rostami and R. Asgari, Phys. Rev. B **91**, 075433 (2015).
[26] A. Pályi and G. Burkard, Phys. Rev. Lett. **106**, 086801 (2011).
[27] Z. Ye, D. Sun, and T. F. Heinz, Nat. Phys. **13**, 26 (2017).
[28] K. Hao, G. Moody, F. Wu, C. K. Dass, L. Xu, C.-H. Chen, L. Sun, M.-Y. Li, L.-J. Li, A. H. MacDonald *et al.*, Nat. Phys. **12**, 677 (2016).
[29] R. Hanson, L. Kouwenhoven, J. Petta, S. Tarucha, and L. Vandersypen, Rev. Mod. Phys. **79**, 1217 (2007).
[30] F. A. Zwanenburg, A. S. Dzurak, A. Morello, M. Y. Simmons, L. C. Hollenberg, G. Klimeck, S. Rogge, S. N. Coppersmith, and M. A. Eriksson, Rev. Mod. Phys. **85**, 961 (2013).
[31] J. R. Petta, A. C. Johnson, J. M. Taylor, E. A. Laird, A. Yacoby, M. D. Lukin, C. M. Marcus, M. P. Hanson, and A. C. Gossard, Science **309**, 2180 (2005).
[32] S. Y. Zhou, G.-H. Gweon, A. Fedorov, P. First, W. De Heer, D.-H. Lee, F. Guinea, A. C. Neto, and A. Lanzara, Nat. Mater. **6**, 770 (2007).
[33] P. Recher, J. Nilsson, G. Burkard, and B. Trauzettel, Phys. Rev. B **79**, 085407 (2009).
[34] G. Sallen, L. Bouet, X. Marie, G. Wang, C. Zhu, W. Han, Y. Lu, P. Tan, T. Amand, B. Liu *et al.*, Phys. Rev. B **86**, 081301 (2012).
[35] K. Wang, T. Taniguchi, K. Watanabe, and P. Kim, arXiv:1610.02929.
[36] L. P. Kouwenhoven, D. Austing, and S. Tarucha, Rep. Prog. Phys. **64**, 701 (2001).
[37] A. Chernikov, T. C. Berkelbach, H. M. Hill, A. Rigosi, Y. Li, O. B. Aslan, D. R. Reichman, M. S. Hybertsen, and T. F. Heinz, Phys. Rev. Lett. **113**, 076802 (2014).
[38] C. Zhao, T. Norden, P. Zhang, P. Zhao, Y. Cheng, F. Sun, J. P. Parry, P. Taheri, J. Wang, Y. Yang, T. Scrace *et al.*, Nature Nanotechnol. (2017), doi:10.1038/nnano.2017.68.
[39] G.-B. Liu, H. Pang, Y. Yao, and W. Yao, New J. Phys. **16**, 105011 (2014).
[40] S. Pavlović and F. Peeters, Phys. Rev. B **91**, 155410 (2015).